Absorbing-generating seaward boundary conditions for fully-coupled hydro-morphodynamical solvers

Article *in* Coastal Engineering · February 2015

DOI: 10.1016/j.coastaleng.2015.02.002

3 authors, including:

R. Briganti
University of Nottingham
44 PUBLICATIONS **464** CITATIONS
SEE PROFILE

Nicholas Dodd
University of Nottingham
87 PUBLICATIONS **1,394** CITATIONS
SEE PROFILE

Absorbing-generating seaward boundary conditions for fully-coupled hydro-morphodynamical solvers

Giorgio Incelli[a,*], Riccardo Briganti[a], Nicholas Dodd[a]

[a] *University of Nottingham, University park, Nottingham, NG7 2RD, UK*

Abstract

This paper presents a new technique to compute open boundary conditions for fully-coupled hydro-morphodynamical numerical solvers based on the Non-Linear Shallow Water and the Exner equations. These conditions allow the generation of incident signals and the absorption of reflected ones, taking into account the bed evolution at the boundary. They use the approximations for linear waves in shallow water and are based on the solution of the Riemann Equations.

The proposed technique is implemented in the fully-coupled hydro-morphodynamical numerical model of Briganti et al. (2012a).

Firstly, the generation and absorption of single monochromatic waves are studied to quantify the error after the reflected wave exited the domain. In all cases the error is always small, giving evidence of the effectiveness of the new seaward boundary conditions.

Furthermore, the propagation and reflection of a monochromatic wave train over a mobile bed are considered. Both flow evolution and bed change are not affected by spurious oscillations when long sequences of waves are tested. Additionally, a very low mobility bed is considered to simulate a 'virtually fixed' bed and new boundary condition results consistently converge to those for the hydrodynamic only case.

Finally, the reflection of a uniform bore over a mobile bed is studied. For this case the Rankine-Hugoniot conditions provide an analytical solution. It is apparent that the adopted linear approximations produce errors in the velocity estimates. Nevertheless, the conditions perform reasonably well even in this demanding non-linear case.

Keywords: fully-coupled, morphodynamics, open boundary, absorbing-generating boundary conditions, morphodynamic bore, Non-Linear Shallow Water Equations, Exner equation

*Corresponding author

Email address: evxgi1@nottingham.ac.uk (Giorgio Incelli)

1. Introduction

In the nearshore region the flow strongly interacts with the bottom sediments, shaping the bed. In the swash zone, in particular, the oscillatory flow and the bed evolve with the same time scale (Kelly & Dodd, 2010). This consideration has led to the development of hydro-morphodynamical numerical models that are able to solve the equations for the flow and bed evolution simultaneously, i.e. enabling full coupling.

In coastal research, fully-coupled solvers are typically applied to a system of equations comprising the Non-Linear Shallow Water Equations (henceforth NLSWEs) and the Exner equation.
Given the limitations of the NLSWEs, these models are frequently forced to locate the seaward boundary at depths where the sediment is still active. Therefore boundary conditions should be able to prescribe the incoming flow and sediment while allowing the outgoing quantities to exit the computational domain. At present, to the best of authors' knowledge, such conditions for fully-coupled models have not been formulated. In morphodynamic numerical models where frequency dispersion is included, it is common practice is to locate the seaward boundary where depth of closure is reached, typically at depths for which the shallow water approximation is no longer appropriate. This occurs with well established solvers, such as Genesis (Hanson & Kraus, 1989) and XBeach (Roelvink et al., 2009), which include sub-models for wave propagation from deep to shallow water.

Fully-coupled models were first used in Hudson & Sweby (2003) and Hudson et al. (2005), who developed a finite volume solver and tested it on a dune migration problem. Later, finite volumes were employed by Dodd et al. (2008) to study the formation of beach cusps. More recently Kelly & Dodd (2010), Briganti et al. (2012b), Zhu et al. (2012) and Zhu & Dodd (2013) used different solvers to simulate bore-driven swash flows. All these works only considered bed load transport. Furthermore, in these works the absorbing-generating seaward boundary conditions have not been used because a single swash event was studied and the seaward boundary was located far from the region of interest so that any reflected perturbation would not interfere with the event considered.

Absorbing-generating conditions are available for the hydrodynamic equations (e.g. Kobayashi et al., 1987; van Dongeren & Svendsen, 1997) and are usually based on the knowledge of the Riemann invariants. They were used also in morphodynamic simulations following a simplified coupled approach (Dodd et al., 2008). Specifically, closure of the problem was achieved by priming the updated bed value at the seaward boundary with that of the first inner cell at the previous time step, i.e. imposing a horizontal bottom therein.
Savary & Zech (2007) presented a fully-coupled characteristic-based approach for boundaries in fluvial environment. This implies that oscillatory flows are not considered. Besides, this technique is suitable for a two fluid layer model,

following the Fraccarollo & Capart (2002) approach, in which a second fluid layer where water and sediment are mixed is considered.

The present study proposes new fully-coupled absorbing-generating seaward boundary conditions for oscillatory flows. These are based on the solution of the Riemann Equations, following previous work by Kelly & Dodd (2009) and Zhu & Dodd (2013). They include approximations for linear waves in shallow water, so that only the incoming water surface perturbation is needed to determine updated quantities at the seaward boundary.

This paper is organised in four sections. Section 1 shows the governing equations, while in Section 2 the new fully-coupled seaward boundary conditions are explained. Section 3 presents the validation tests and Section 4 summarizes the achieved results.

2. Governing Equations

2.1. Definitions

The model used in this study solves the one-dimensional NLSWEs coupled with the Exner sediment continuity equation for the bed evolution.
The above-mentioned equations form a system of conservation laws with source terms:

$$\begin{bmatrix} h \\ uh \\ z_b \end{bmatrix}_t + \begin{bmatrix} uh \\ hu^2 + \frac{1}{2}gh^2 \\ \xi q_s \end{bmatrix}_x = \begin{bmatrix} 0 \\ -gh\frac{\partial z_b}{\partial x} \\ 0 \end{bmatrix}, \tag{1}$$

where x and t are the independent variables (space and time respectively). g is the gravitational acceleration. h, u and z_b are the dependent variables, namely the local water depth, the depth-averaged horizontal velocity and the bed level in the order. Figure 1 shows the variables of the hydro-morphodynamic system.

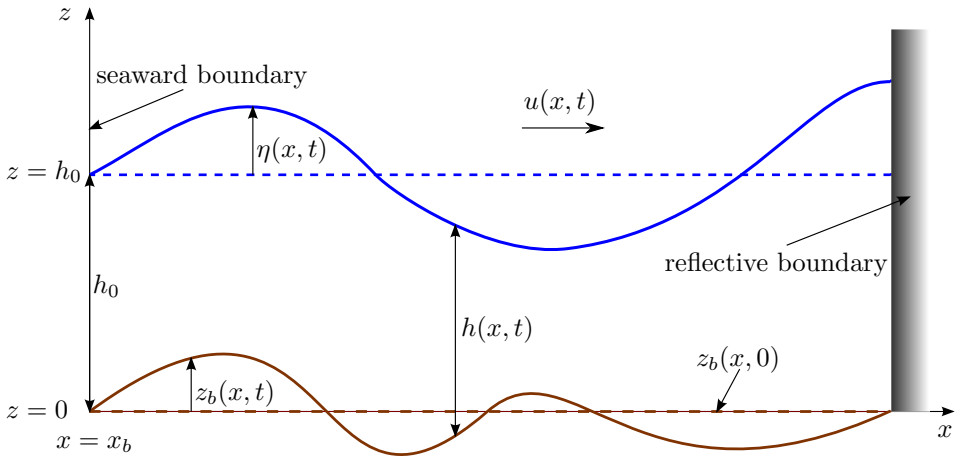

Figure 1: Sketch of variables for a generic mobile bed problem with a seaward (left) boundary and a reflective (right) one.

Additionally, $\xi = 1/(1 - p_b)$, where p_b is bed porosity, and q_s is the instantaneous bed load sediment transport, for which the well-known Grass formula is used

$$q_s = Au^3, \tag{2}$$

with A being a sediment mobility parameter. Note that bed load sediment transport is appropriate for medium-coarse sand environments.

System (1) is solved using the TVD-MacCormack scheme (hereinafter TVD-MCC) from Briganti et al. (2012a), which is restated in Appendix A.

3. Fully-coupled seaward boundary conditions

3.1. Formulation of conditions

In this section, the new fully-coupled absorbing-generating seaward boundary conditions, named a Riemann Equation Boundary Conditions (henceforth REBCs), are presented.

The NLSWEs-Exner system (1) is rewritten in primitive form:

$$\begin{bmatrix} h \\ u \\ z_b \end{bmatrix}_t + \begin{bmatrix} hu \\ \frac{1}{2}u^2 + g(h+z_b) \\ \xi q_s \end{bmatrix}_x = \begin{bmatrix} 0 \\ 0 \\ 0 \end{bmatrix}. \tag{3}$$

It is assumed that the flow at the seaward boundary is subcritical and that approximations for linear waves in shallow water can be used therein. These are essentially the same assumptions made in Kobayashi et al. (1987).
The seaward boundary is located at $x = x_b$ and the incoming waves propagate from the left to the right of Figure 1. Thus $h(x_b, t)$ can be computed from

$$h(x_b, t) = h_0 + z_b(x_b, 0) - z_b(x_b, t) + \eta_i(x_b, t) + \eta_r(x_b, t), \tag{4}$$

where h_0 is the still water depth at the seaward boundary and η is the perturbation from the initial water surface (i.e. $h_0 + z_b(x_b, 0)$) due to the incident (η_i) and reflected (η_r) waves respectively. In particular, $\eta_i(x_b, t)$ is known while the initial reference bed level is set $z_b(x_b, 0) = 0$ (see Figure 1) and therefore omitted in the following.
The water velocity at the seaward boundary $u(x_b, t)$ can be computed as

$$u(x_b, t) = u_i(x_b, t) + u_r(x_b, t)\ , \tag{5}$$

with

$$u_i(x_b, t) \approx \quad \eta_i(x_b, t)\sqrt{\frac{g}{h_0 - z_b(x_b, t)}}, \tag{6}$$

$$u_r(x_b, t) \approx -\eta_r(x_b, t)\sqrt{\frac{g}{h_0 - z_b(x_b, t)}}. \tag{7}$$

$u_i(x_b, t)$ is a function of $\eta_i(x_b, t)$, which is known, and $z_b(x_b, t)$. $u_r(x_b, t)$ is related to $z_b(x_b, t)$ and $\eta_r(x_b, t)$ through relationship (7). The new technique makes use of two of the three Riemann Equations associated to system (3) at the seaward boundary to determine two unknowns, $z_b(x_b, t)$ and $\eta_r(x_b, t)$, with the help of relationships (4), (6) and (7).

The generic Riemann Equation (see Zhu, 2012 for the derivation) is written as:

$$\Re^k = \frac{Dz_b}{Dt} + \frac{\lambda_k}{\lambda_k - u}\frac{Dh}{Dt} + \frac{\lambda_k}{g}\frac{Du}{Dt} = 0, \tag{8}$$

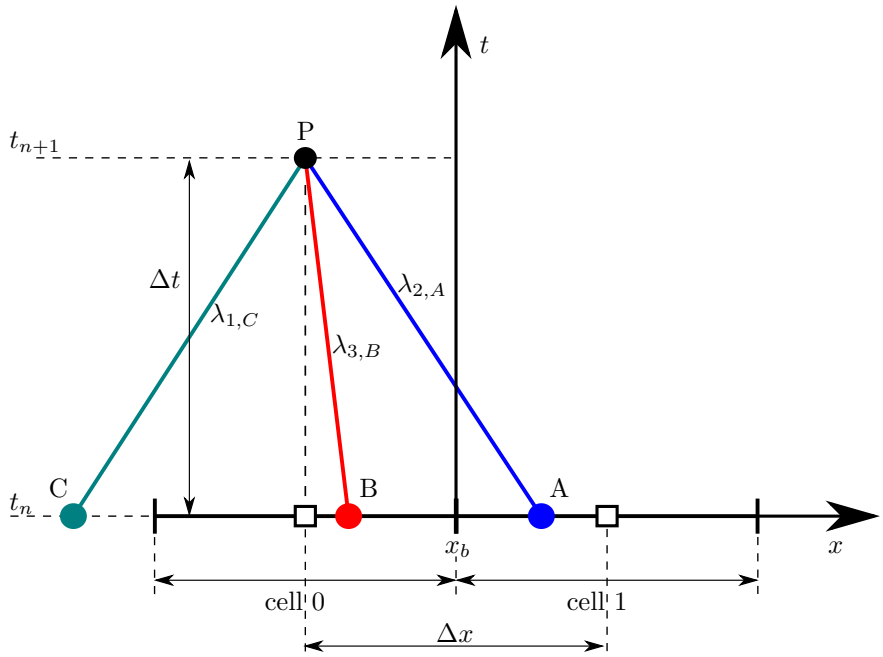

Figure 2: Sketch for fully-coupled seaward boundary conditions. Empty squares on x axis indicate cell centres.

where $\frac{D\cdot}{Dt}$ indicates the total (material) derivative and λ_k ($k = 1, 2, 3$) are the eigenvalues of the Jacobian matrix associated to system (3). Such eigenvalues are computed numerically (e.g. Kelly & Dodd, 2009) as no analytical expression is available for the morphodynamic problem.
At the seaward boundary, λ_1 is positive, λ_2 negative, while:

$$\lambda_3 > 0 \quad \text{if} \quad u > 0\,,$$
$$\lambda_3 < 0 \quad \text{if} \quad u < 0\,.$$

A sketch to illustrate the new technique is provided in Figure 2, where two cells and their centres are indicated. In fact, the domain length L_x is divided in M control volumes or cells of equal width Δx, so that $L_x = M\Delta x$. Note that the TVD-MCC is a hybrid scheme, as the original MCC is a finite difference scheme whilst the TVD correction needs the knowledge of quantities at numerical cell interfaces. Thus, it is more convenient to refer to a finite volume domain division in cells assuming constant dependent variable values in each cell and its centre coincident with a node in the finite difference framework.
The physical seaward boundary is set as the left edge of cell 1. Cell 0 is the one at which the new boundary conditions are prescribed. Two consecutive time levels are involved here, i.e. n and $n+1$. P is the centre of cell 0 at time t_{n+1}, where dependent variables (h, u and z_b) require updating.
Only $\lambda_{2,A}$ and $\lambda_{3,B}$ are needed. They originate from points A and B (both to be located) at time t_n and pass through P at time t_{n+1}. Therefore, only the

Riemann Equations for $k = 2, 3$ will be used. They form a determined system of two equations in two unknowns ($z_{b,P}$ and $\eta_{r,P}$). Note that $z_{b,P} = z_b(P(x = x_P, t = t_P = t_{n+1}))$.
Dependent variable values are available at time t_n at each cell centre. At a given time, variable and eigenspeed values are assumed to vary smoothly in space so that linear interpolation between cells 0 and 1 gives reasonable accuracy.

The procedure starts by estimating x_A and x_B. Subsequently, values for h, u and z_b at these two points are computed. Although A and B spatial coordinates are unknown, the Courant Number condition assures that $|\lambda_k|\Delta t < \Delta x$, where Δt is the time step. Hence, the following iterative method is employed (described for one eigenspeed only because the other is analogous):

1. λ_2 eigenspeeds at centres of cells 0 and 1 are computed ($\lambda_{2,0}$ and $\lambda_{2,1}$) from dependent variables at time t_n;
2. initial guesses for x_A and $\lambda_{2,A}$ are made: $x_A = x_P + \frac{\Delta x}{2}$ and $\lambda_{2,A} = \frac{\lambda_{2,0}+\lambda_{2,1}}{2}$;
3. a new estimate for x_A is computed using the additional relationship $x_{A,new} = x_P - \lambda_{2,A}\Delta t$;
4. the relative error ϵ_A between $x_{A,new}$ and x_A, defined as

$$\epsilon_A = \frac{x_{A,new} - x_A}{x_A},$$

is compared with a tolerance value ($tol = 10^{-2}$):

- if $\epsilon_A < tol$, then variable values ($h_A, u_A, z_{b,A}$) are computed with linear interpolation between those at cells 0 and 1;
- if $\epsilon_A > tol$, then a bisection method is undertaken: new x_A and $\lambda_{2,A}$ values are computed and the process goes back to point 3.

Note that if $\lambda_{3,B} > 0$, then values will be extrapolated rather than interpolated from those at cell centres 0 and 1. As $|\lambda_3| \ll |\lambda_{1,2}|$, the error related to the extrapolation is assumed to be negligible.
Once dependent variables at A and B are known, the Riemann Equations can be solved:

$$(z_{b,P} - z_{b,A}) + \mu_{2,A}(h_P - h_A) + \omega_{2,A}(u_P - u_A) = 0, \tag{9}$$
$$(z_{b,P} - z_{b,B}) + \mu_{3,B}(h_P - h_B) + \omega_{3,B}(u_P - u_B) = 0, \tag{10}$$

where

$$\mu_{k,j} = \frac{\lambda_{k,j}}{\lambda_{k,j} - u_j}, \tag{11}$$
$$\omega_{k,j} = \frac{\lambda_{k,j}}{g}, \tag{12}$$

with $(k,j) = [(2,A),(3,B)]$. The aforementioned equations can be rearranged in this way:

$$z_{b,P} + \mu_{2,A} h_P + \omega_{2,A} u_P = S_A, \tag{13}$$
$$z_{b,P} + \mu_{3,B} h_P + \omega_{3,B} u_P = S_B, \tag{14}$$

where

$$S_j = \left(z_{b,j} + \mu_{k,j} h_j + \omega_{k,j} u_j\right), \text{ with } (k,j) = [(2,A),(3,B)].$$

It is convenient to subtract equation (14) from (13) to eliminate $z_{b,P}$:

$$\mu h_P + \omega u_P = S, \tag{15}$$

with

$$\mu = \mu_{2,A} - \mu_{3,B} \ ,$$
$$\omega = \omega_{2,A} - \omega_{3,B} \ ,$$
$$S = S_A - S_B.$$

Equations (4),(5),(6) and (7) are substituted into (13) and (15) to obtain a system of two equations in the unknowns $z_{b,P}$ and $\eta_{r,P}$:

$$\begin{aligned} z_{b,P} + \mu_{2,A} \left(h_0 - z_{b,P} + \eta_{i,P} + \eta_{r,P}\right) + \\ + \omega_{2,A} \sqrt{\frac{g}{h_0 - z_{b,P}}} \left(\eta_{i,P} - \eta_{r,P}\right) = S_A, \end{aligned} \tag{16}$$

$$\begin{aligned} \mu \ \left(h_0 - z_{b,P} + \eta_{i,P} + \eta_{r,P}\right) + \\ + \omega \ \sqrt{\frac{g}{h_0 - z_{b,P}}} \left(\eta_{i,P} - \eta_{r,P}\right) = S. \end{aligned} \tag{17}$$

An auxiliary variable is defined as

$$\Omega \ = \ \sqrt{h_0 - z_{b,P}} \quad .$$

Note that $\Omega \ > \ 0$ by definition (see Figure 1).
Then $\eta_{r,P}$ is obtained from equation (17):

$$\eta_{r,P} = \eta_{i,P} + \Omega \, \frac{S - \mu \left(\Omega^2 + 2\eta_{i,P}\right)}{\Omega\mu - \sqrt{g}\omega} \tag{18}$$

and substituted into equation (16), obtaining a cubic equation in Ω:

$$\Omega^3 + a_1 \Omega^2 + a_2 \Omega + a_3 = 0, \tag{19}$$

where

$$a_1 = \frac{\sqrt{g}\left(\omega - \omega\mu_{2,A} + \mu\omega_{2,A}\right)}{(-\mu)}, \tag{20}$$

$$a_2 = \frac{\left(\mu h_0 - \mu S_A + S\mu_{2,A}\right)}{(-\mu)}, \tag{21}$$

$$a_3 = \frac{\sqrt{g}\left(\omega S_A - S\omega_{2,A} - \omega h_0 + 2\eta_{i,P}\left(\mu\omega_{2,A} - \omega\mu_{2,A}\right)\right)}{(-\mu)}. \tag{22}$$

Equation (19) is solved through Cardano's formula (Abramowitz & Stegun, 1972); when there are three real roots, the one that yields the closest value of $z_{b,P}$ to the former at previous time t_n is used as the updated bed level.
At this point, $\eta_{r,P}$ is computed from equation (18) and the dependent variables at the seaward boundary cell are updated by means of (4) and (5).

In order to refine the obtained boundary values, an iterative process is introduced. New eigenspeed values $\lambda_{k,P}$ are computed from h_P, u_P and $z_{b,P}$, and then averaged with the previously estimated ones:

$$\lambda_{2,AP} = \frac{\lambda_{2,A} + \lambda_{2,P}}{2},$$
$$\lambda_{3,BP} = \frac{\lambda_{3,B} + \lambda_{3,P}}{2}.$$

These averages are used to update coefficients (11) and (12), together with the following averaged velocity values:

$$u_{jP} = \frac{u_j + u_P}{2} \quad \text{with } j = A, B.$$

Hence, Riemann Equations (9) and (10) are solved again and new dependent variable values at P are available. This process can be repeated until subsequent values of h_P, u_P and $z_{b,P}$ agree to a prescribed degree of accuracy.
In particular, it is convenient to define a relative error on h_P as

$$\epsilon_h = \frac{h_{P,new} - h_{P,old}}{h_{P,old}},$$

with *new* and *old* labelling the last and the second last computed values for h_P respectively. Iteration is then terminated when $|\epsilon_h| < 10^{-12}$.

4. New boundary condition validation

4.1. Introduction

Seaward boundary conditions are often validated against tests of reflection of sinusoidal waves (e.g. Wei et al., 1999). Although analytical solutions exist for reflection over a fixed bed, none is available in the literature for a mobile bed case.

The validation presented here comprises a group of tests involving monochromatic waves and one for moving discontinuities, i.e. uniform bores.

The first test considers the full reflection of a single monochromatic wave over a mobile bed. This test aims at quantifying the capability of the REBCs to allow reflected signals to exit the domain.

The second test involves a monochromatic wave train over a mobile bed. Complete reflection at one end of the physical domain leads to the establishment of standing waves. The purpose of this test is to check whether the evolution of the bed is affected by the REBCs or not.

Thirdly, tests of a monochromatic wave train over 'virtually fixed' and fixed beds are shown. These tests aim at confirming the convergence of the fully-coupled boundary conditions to hydrodynamic only ones when the bed mobility tends to zero.

Finally, for a uniform bore over a mobile bed, the Rankine-Hugoniot conditions provide an exact solution (Kelly & Dodd, 2010). Therefore, a further test involving the reflection of a morphodynamic bore is studied. This case is very demanding for the REBCs, as in shocks the particle velocity departs from the approximation for linear waves in shallow water (relationships (6) and (7)) adopted in the new boundary conditions. It is thus a useful test for the robustness of the REBCs.

Note that all simulations were carried out for inviscid fluid only, as often in previous works with NLSWEs (e.g. Kelly & Dodd, 2010 and Briganti et al., 2012b among others). In fact, including bottom friction would mask potential spurious oscillation introduced by the REBCs.

4.2. Monochromatic wave tests

This group of tests considered a single monochromatic wave or a monochromatic wave train entering an initially flat bottomed channel with uniform still water depth h_0.

The input signal was a monochromatic wave of height H, period T and wavelength L. The tests were always carried out within the shallow water limit, i.e. $h_0/L < 1/20$ (Svendsen, 2005). Furthermore, the authors decided to test less steep waves to limit their steepening caused by the adoption of the NLSWEs, so that wave breaking was avoided. Breaking waves (bores) are considered in Subsection 4.3.

For the mobile and the virtually fixed bed tests, the sediment mobility parameter A in the Grass formula was set at $4 \times 10^{-3}\ s^2/m$ and at $1 \times 10^{-8}\ s^2/m$ respectively, following Kelly & Dodd (2009) and Briganti et al. (2012a).

As stated in Subsection 3.1, the domain was divided in M equal cells. Two ghost cells were used to impose the boundary conditions: cell 0 for the seaward (left) boundary, where REBCs were prescribed, and cell $M+1$ for fully reflective conditions at the right boundary. These latter read:

$$h_{M+1} = \quad h_M \ , \tag{23}$$

$$u_{M+1} = -u_M \ , \tag{24}$$

$$z_{b,M+1} = \quad z_{b,M} \ . \tag{25}$$

With reference to the numerical setup, a spatial step size Δx of 0.10 m and a Courant Number CN of 0.90 were chosen.

165

4.2.1. Single monochromatic wave over a mobile bed

The test with a single monochromatic wave was performed using the settings shown in Table 1.

Domain length	L_x	m	100.00			
Still water depth	h_0	m	0.5	1.0	2.0	5.0
Incoming wave period	T	s	45.16	31.93	22.58	14.28
Incoming wave length	L	m	100.00			
Incoming wave height	H	m	0.02	or 0.05	or	0.10
Sediment mobility parameter	A	s^2m^{-1}	4×10^{-3}			
Spatial step size	Δx	m	0.10			
Courant Number	CN	$-$	0.90			
Duration of the simulations	$-$	s	$> 4\,T$			

Table 1: Single monochromatic wave over a mobile bed - test settings.

The aim of this test is to provide a quantification of the error in absorption produced by the application of the REBCs and to understand if and how it varies with the ratios h_0/L and H/L, i.e. relative wavenumber and wave steepness. Their variation was obtained by fixing L and changing values of h_0 and H. The values for h_0 and H were selected to let the parameters h_0/L and H/L span an order of magnitude.
Firstly, four different values for h_0 were chosen, corresponding to four different incoming wave periods T for fixed L (periods were computed through the dispersion relationship for linear waves in shallow water). Secondly, three values of H were adopted (see Table 1).
In this test the domain is long enough so that the generation of the incoming signal at the seaward boundary ceases before the absorption of the reflected wave begins. Some snapshots of Video 1 (available for the online version of this paper) are provided in Figure 3 to illustrate the physical evolution of the flow and bed in this test. The final bed profile shows respectively one erosional and one depositional area moving away from the right boundary. If a single wave with a leading trough is simulated instead, the order of the areas is reversed

(results not showed here).
Any wave that enters the domain should eventually exit from the seaward boundary, leaving a quiescent flow state behind (see top panel for time 100 s of Figure 3). From the time history of $\eta_{r,P}$ it is possible to identify the time level after which its value falls below a defined threshold, so that the reflected wave can be assumed to be completely transmitted through the seaward boundary. For this test the threshold was set at 1/1000 of the maximum absolute value of $\eta_{i,P}$, i.e. $H/2$. Then, maximum and minimum values for water surface perturbation and velocity in the whole domain were recorded after the absorption terminated. We define the following non-dimensional estimates of (local) error:

$$\eta^* = \frac{\eta_m}{H/2} \,,$$
$$u^* = \frac{u_m}{u_{i,max}} \,,$$

where η_m and u_m refer to the above maximum (or minimum) values, detected at a certain cell m, while $u_{i,max}$ is the maximum velocity of the particular incoming wave of height H. In Figure 4 it is apparent that $|\eta^*|$ and $|u^*|$ decrease as relative wavenumber increases and rise with incoming wave steepness. Local errors for case with $h_0/L = 0.005$ and $H = 0.10\ m$ are included in Figure 4 for completeness, although in this case the sinusoidal wave clearly broke, generating a bore (not showed here) and deteriorating the performance of REBCs. This is the only case among those tested in which breaking occurred. In all remaining cases the local errors are small and within the 1% threshold.
Figure 5 shows the root mean squared errors (RMSE) for water surface perturbation and velocity, computed throughout the domain. The RMSE definition is:

$$\mathrm{RMSE}(q) = \left(\frac{1}{M} \sum_{m=1}^{M} (q_m - \tilde{q})^2 \right)^{\frac{1}{2}} \tag{26}$$

where q indicates a generic quantity (η or u for this test), $\tilde{q}$ is the corresponding expected value (which is zero for both η or u in this case) and m stands for the particular cell. These RMSE results confirm that errors decrease as h_0/L increases and rise with H values. Moreover, the errors remain at least 2 orders of magnitude smaller than the respective maximum incoming signal, indicating that the developed seaward boundary conditions are effective.

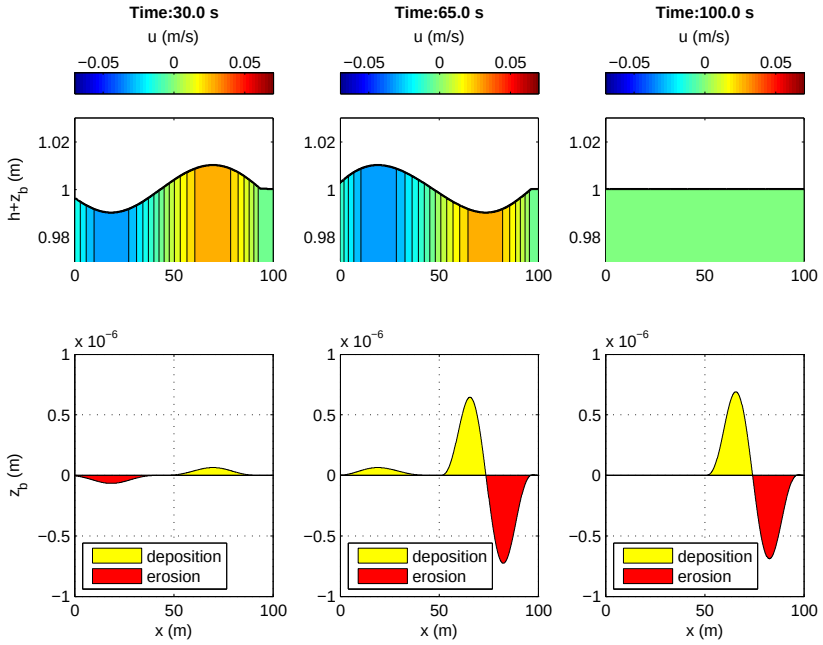

Figure 3: Single monochromatic wave over a mobile bed - Video 1 snapshots at three different times - $h_0 = 1.0\ m$, $T = 31.93\ s$ and $H = 0.02\ m$. Top panels: water surface ($h + z_b$) profiles with water velocity (u) contours; bottom panels: bed level (z_b) profiles.

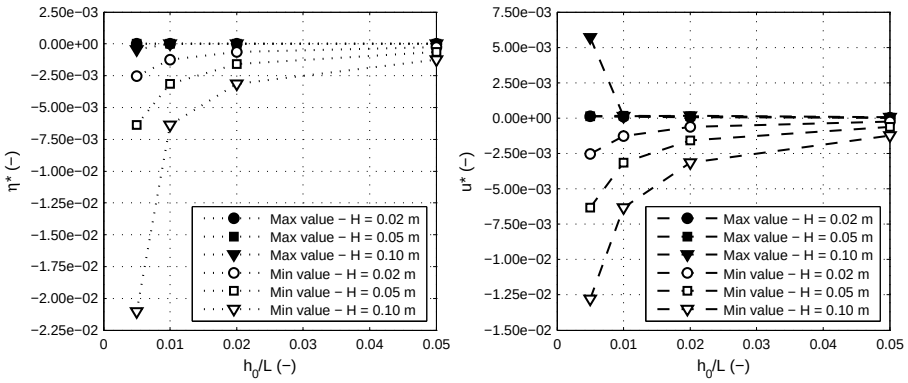

Figure 4: Single monochromatic wave over a mobile bed. Maximum and minimum non-dimensional values for water surface perturbations (η^*) and velocity (u^*) with respect to h_0/L for given H values.

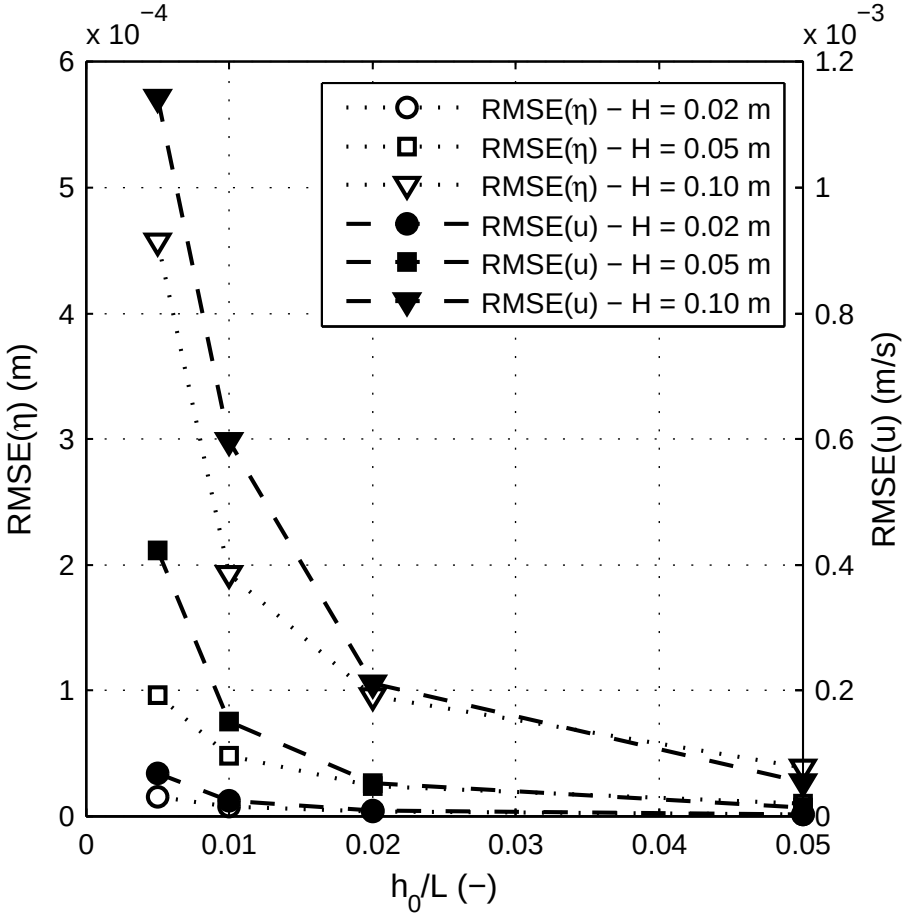

Figure 5: Single monochromatic wave over a mobile bed. Root mean squared errors for water surface perturbation (RMSE(η)) and velocity (RMSE(u)) with respect to h_0/L for given H values.

4.2.2. Monochromatic wave train over a mobile bed

This test was carried out with the settings summarised in Table 2.

Domain length	L_x	m	200.00
Still water depth	h_0	m	0.5 1.0
Incoming wave period	T	s	45.16
Incoming wave length	L	m	100.00 141.42
Incoming wave height	H	m	0.02
Sediment mobility parameter	A	s^2m^{-1}	4×10^{-3}
Spatial step size	Δx	m	0.10
Courant Number	CN	$-$	0.90
Duration of the simulation	$-$	s	2×10^5

Table 2: Monochromatic wave train over a mobile bed - test settings.

As shown in Table 2, two different values for the still water depth h_0 were considered, namely 0.5 m and 1.0 m, which correspond to wavelengths L of 100.00 m and 141.42 m respectively. The domain length was chosen in order to be long enough to contain at least one wavelength.

Videos 2 and 3 (available for the online version of this paper) illustrate the physical evolution of the flow and bed for both cases. The monochromatic wave train generates a non-linear standing wave pattern and a corresponding pattern in the bed profile.

Figures 6 and 7 display water depth, velocity and bed level time stacks. Water depth and velocity ones show the effects of non-linearity, that is the wave steepening, which is exacerbated with smaller h_0. Those of the bed level exhibit the long-term stability in time of the solution for the bed profile. The bedforms develop and remain almost stationary, consistently with the nature of the hydrodynamic field. Only small oscillations due to the non-linearity of the waves occur.

Panels (a) and (c) of Figure 8 present the final bed level profiles for both cases, better showing the bed pattern, which comprises a sequence of deposition-erosion-deposition areas and two zero-bed-change points every half wavelength. This pattern is not altered by the location of the seaward boundary, even when the latter is set at a non-integer multiple of L, and therefore the REBCs act effectively as a 'transparent' boundary.

In contrast with linear theory, the non-linearity of the waves causes oscillation of the nodal points and asymmetry in the deposition/erosion pattern. The more the wave steepens, that is in the direction of decreasing x, the more the velocity nodes oscillate and the bed profile is affected, showing a small accretion between consecutive depositional areas (for example see panel (a) of Figure 8).

However, the focus of this paper is on the seaward boundary conditions and it is important to highlight that no significant spurious oscillation is generated at the seaward boundary and propagates into the bed level, i.e. bed level time contours are substantially parallel to time axis.

Panels (b) and (d) of Figure 8 present the amplitudes of the first two harmonics

of the surface standing wave for both cases. The depositional areas occur at both sides of each wave antinode position while the erosional trough is apparent where wave nodes are located.

It is very interesting to note analogies with the experimental results of Figure 4, panel (e), of Landry et al., 2007, showing the final profile of a fine sand bed which underwent standing wave action for 7.0 days. The bottom evolution pattern obtained in the present test qualitatively agrees with that of the reference figure, although ripples are not modelled here. Additionally, Landry et al. (2007) explicitly mention vertical water velocities and suspended sediment transport, which are not included in the present model.

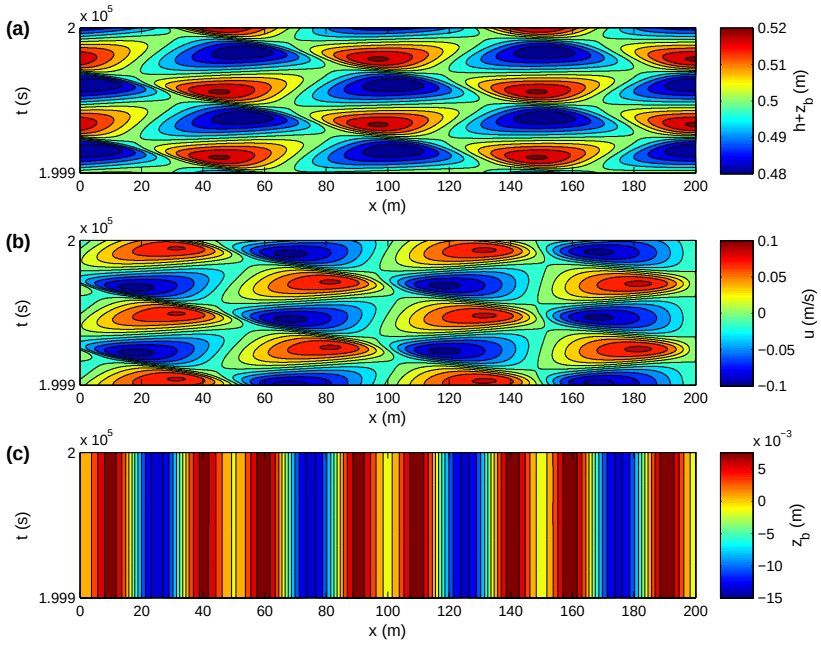

Figure 6: Monochromatic wave train over a mobile bed - time stacks - $h_0 = 0.5\ m$, $T = 45.16\ s$ and $H = 0.02\ m$. Panel (a): water surface ($h + z_b$); panel (b): velocity (u); panel (c): bed level (z_b).

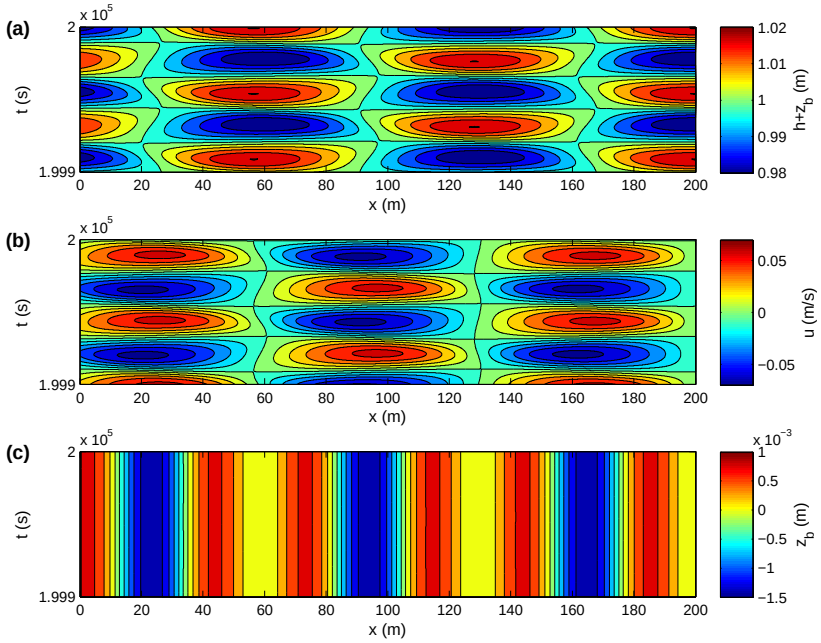

Figure 7: Monochromatic wave train over a mobile bed - time stacks - $h_0 = 1.0\ m$, $T = 45.16\ s$ and $H = 0.02\ m$. Panel (a): water surface ($h + z_b$); panel (b): velocity (u); panel (c): bed level (z_b).

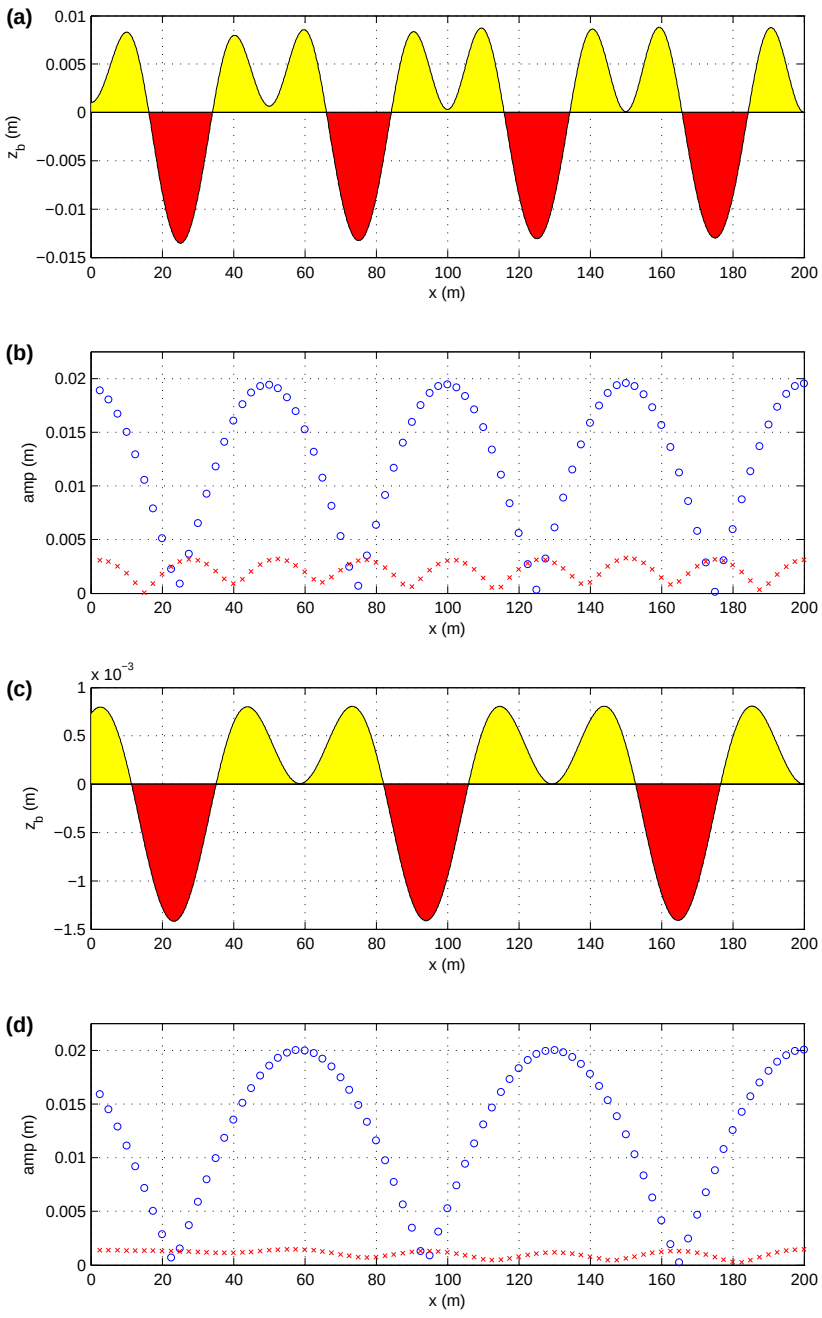

Figure 8: Monochromatic wave train over a mobile bed - $T = 45.16\ s$ and $H = 0.02\ m$. Panels (a) and (b): $h_0 = 0.5\ m$; panels (c) and (d): $h_0 = 1.0\ m$. Panels (a) and (c): final bed level (z_b) profile at $t = 2 \times 10^5\ s$, depositional and erosional areas are filled in yellow and red respectively; panels (b) and (d): amplitudes (amp) of first two harmonics of the surface standing wave.

4.2.3. Monochromatic wave train over virtually fixed and fixed bed

These tests were performed with the settings shown in Table 3.

Domain length	L_x	m	200.00
Still water depth	h_0	m	0.5
Incoming wave period	T	s	45.16
Incoming wave length	L	m	100.00
Incoming wave height	H	m	0.02
Sediment mobility parameter	A	s^2m^{-1}	1×10^{-8}
Spatial step size	Δx	m	0.10
Courant Number	CN	$-$	0.90
Duration of the simulation	$-$	s	1000

Table 3: Monochromatic wave train over virtually fixed and fixed bed - test settings.

As reported in Table 3, the still water depth h_0 was set at 0.5 m, which corresponds to a wavelength L of 100.00 m.

For the virtually fixed bed simulation $A = 1 \times 10^{-8}$ s^2/m, following Briganti et al. (2012a). The fixed bed case was obtained by running the solver for the NLSWEs only and applying the hydrodynamic only conditions of Kobayashi et al. (1987) at seaward boundary. The scope of these tests is to check if, when A is very small, the results obtained with the REBCs converge to those for the hydrodynamic only case.

Figure 9 presents water surface time stacks for the virtually fixed and fixed bed simulations. Firstly, panel (a) shows results obtained using the REBCs for a virtually fixed bed. Secondly, panel (b) displays results achieved using the hydrodynamic only boundary conditions for a fixed bed. Finally, panel (c) shows results obtained with Kobayashi et al. (1987) conditions for fixed bed and employing a different hydrodynamic solver, namely the finite volume solver from Briganti & Dodd (2009), based on the Weighted Average Flux (or WAF) method (Toro, 2001).

Figure 9 displays excellent consistency of the results, with differences in water surface values of the order of 10^{-4} m among the three cases. This figure shows that the (morphodynamic) virtually fixed bed case converges to the (hydrodynamic) fixed bed one and indicates that in this limit the REBCs converge to the hydrodynamic only boundary conditions. Moreover, the solution for the fixed bed case is confirmed by that obtained using the finite volume solver. In the light of this, we firmly maintain that result features, for instance wave steepening and node oscillations, are not introduced by the REBCs or scheme-specific.

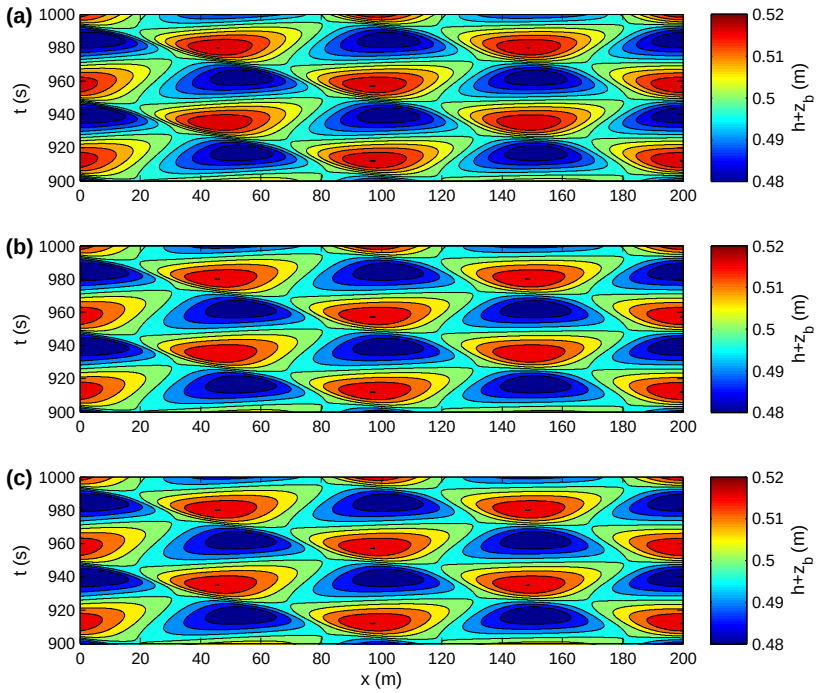

Figure 9: Monochromatic wave train over virtually fixed and fixed bed - water surface ($h+z_b$) time stacks - $h_0 = 0.5\ m$, $T = 45.16\ s$ and $H = 0.02\ m$. Panel (a): REBCs, virtually fixed bed and TVD-MCC; panel (b): hydrodynamic seaward boundary conditions, fixed bed and TVD-MCC; panel (c): hydrodynamic seaward boundary conditions, fixed bed and WAF method solver.

4.3. Morphodynamic bore test

This test involved the reflection of a uniform bore using the settings shown in Table 4.

Domain length	L_x	m	10.00
Still water depth	h_0	m	1.0
Sediment mobility parameter	A	$s^2 m^{-1}$	4×10^{-3}
Spatial step size	Δx	m	0.01
Courant Number	CN	$-$	0.80
Duration of the simulation	$-$	s	10

Table 4: Morphodynamic bore - test settings.

The domain consisted of an initially flat bottomed channel with an erodible bed. The still water depth h_0 was set at 1.0 m while the incoming bore height H at 0.20 m.
As previously for the wave test over a mobile bed, the parameter A was chosen equal to 4×10^{-3} s^2/m.
The boundary conditions were the REBCs on the left of the domain and the reflective ones on the right.
With reference to the numerical setup, a spatial step size Δx of 0.01 m and a Courant Number CN of 0.80 were adopted for this test.
The exact solutions are calculated from the Rankine-Hugoniot conditions and in theory the simulation should reproduce three distinct phases:

1. an incoming bore advancing rightward with the following left side values:

$$h = 1.200\ m\ , \tag{27}$$
$$u = 6.002 \times 10^{-1}\ m/s\ , \tag{28}$$
$$z_b = 4.003 \times 10^{-4}\ m\ ; \tag{29}$$

2. a reflected bore advancing leftward with the following right side values:

$$h = 1.418\ m\ , \tag{30}$$
$$u = 0.000\ m/s\ , \tag{31}$$
$$z_b = 8.373 \times 10^{-4}\ m\ ; \tag{32}$$

3. a restored quiescent flow state where dependent variables assume the right side values of phase 2 throughout the domain.

Figure 10 provides three snapshot columns (one for each of phase) of Video 4 (available for the online version of this paper) to describe the physical evolution of this test.
It is apparent that when the reflected bore reaches the seaward domain, it is not fully absorbed and a part of it propagates back into the domain (see for instance top panel for time 7.00 s in Figure 10). To provide a quantification of

the absorption defect, the (negative) water velocity value retained in the domain is 6.83% of (28).
It is known that the approximations for linear waves in shallow water included in the REBCs, namely relationships (6) and (7), do not suit the bore case, as they produced non-negligible errors in the water velocity estimates. For example, the incoming bore velocity using (6) is $6.277 \times 10^{-1}\ m/s$, introducing an absolute error of $0.275 \times 10^{-1}\ m/s$ and a relative one of 4.58% with respect to the exact one, that is (28).
The authors investigated the aforementioned issues simulating a range of bores of different heights. Two errors were studied and their behaviours with respect to relative incoming bore heights (H/h_0) are provided in Figure 11.
Firstly, ϵ_{inc} is a quantification of the error related to the adoption of approximations for linear waves in shallow water. It is defined as the relative error of the approximate incoming bore velocity with respect to the exact one:

$$\epsilon_{inc} = \frac{u_{i,approx} - u_{i,exact}}{u_{i,exact}}.$$

Secondly, ϵ_{ret} is an estimate of the absorption defect. It is calculated as the ratio between the minimum (as it is negative) water velocity value retained in the domain (after the reflected bore reached the seaward boundary) and the incoming bore exact one:

$$\epsilon_{ret} = \frac{u_{retained}}{u_{i,exact}}.$$

Figure 11 shows that ϵ_{inc} is roughly half of the corresponding ϵ_{ret} and that both errors consistently tend to zero with H/h_0.

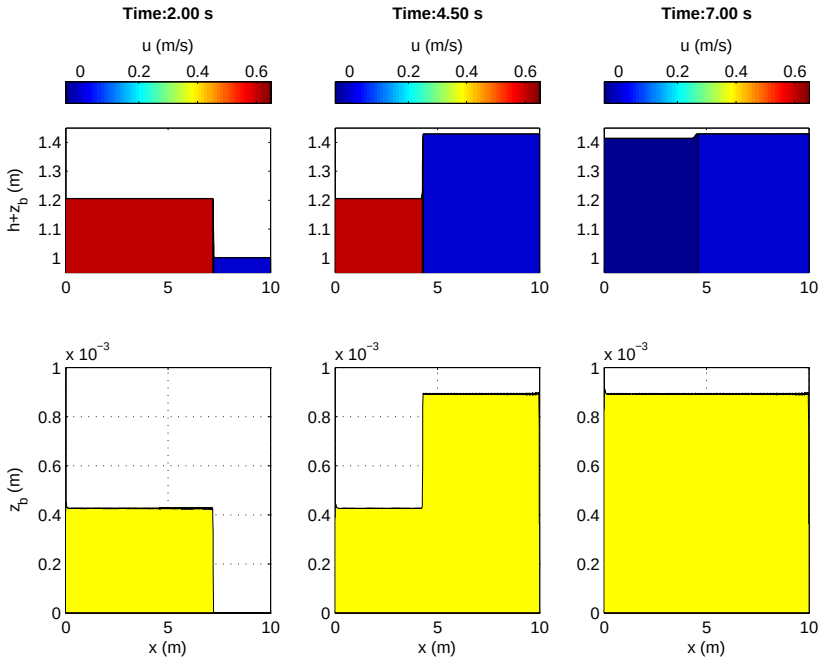

Figure 10: Morphodynamic bore - Video 4 snapshots at three different times - $h_0 = 1.0\ m$ and $H = 0.20\ m$. Top panels: water surface ($h + z_b$) profiles with water velocity (u) contours; bottom panels: bed level (z_b) profiles.

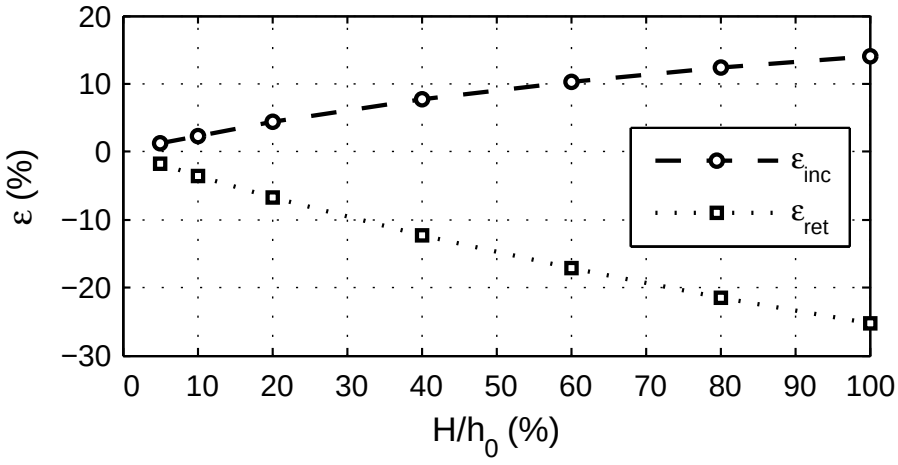

Figure 11: Morphodynamic bore - error analysis. Behaviour of the error related to the adoption of approximations for linear waves in shallow water (ϵ_{inc}) and of the absorption defect one (ϵ_{ret}) with respect to relative incoming bore height (H/h_0).

In particular, for $H = 0.05\ m$, $\epsilon_{inc} \approx 1.00\%$ and the new exact solutions are:

1. for the incoming bore left side (advancing rightward):

$$h = 1.050\ m\ , \tag{33}$$
$$u = 1.547 \times 10^{-1}\ m/s\ , \tag{34}$$
$$z_b = 7.599 \times 10^{-6}\ m\ ; \tag{35}$$

2. for the reflected bore right side (advancing leftward):

$$h = 1.101\ m\ , \tag{36}$$
$$u = 0.000\ m/s\ , \tag{37}$$
$$z_b = 1.538 \times 10^{-5}\ m\ . \tag{38}$$

Figure 12 shows that the REBCs give reasonably good results for $H = 0.05\ m$ and this is confirmed by the fact that ϵ_{ret} falls from 6.83% of the previous case to 1.82% of the present one.

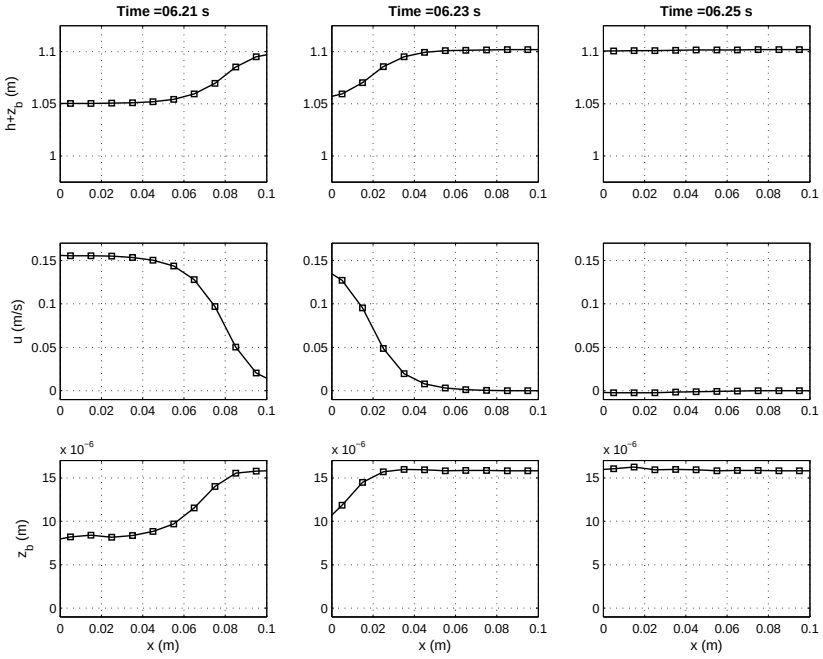

Figure 12: Morphodynamic bore - profiles in the proximity of the seaward boundary at three different times around time of reflected bore arrival therein - $h_0 = 1.0\ m$ and $H = 0.05\ m$. Top panels: water surface ($h + z_b$); mid panels: velocity (u); bottom panels: bed level (z_b).

Further simulations (not shown here) demonstrate that reducing the Courant Number or increasing the spatial resolution (i.e. adopting a smaller Δx) do not improve the results significantly. Moreover, even switching from the adopted flux limiter (Minmod, see Appendix A) to others, for example Superbee or van Leer ones (Sweby, 1984), do not yield substantial changes.

In addition to this, a test over a virtually fixed bed was carried out and it confirms substantially the same amount of ϵ_{ret} for each bore height previously simulated over a mobile bed.

Although the focus of the present work is on the seaward boundary, the results in Video 4 show a numerical error in the bed profile at the reflective boundary, i.e. after the reflection of the incoming bore the bed does not reach the right final value but remains substantially lower therein. The authors could not solve this issue but studied it in detail and concise analysis and discussion are provided in Appendix B.

5. Discussion and conclusions

This paper presents a novel technique for deriving fully-coupled absorbing-generating seaward boundary conditions for the NLSWEs-Exner equation system. Riemann Equations and approximations for linear waves in shallow water are employed. The REBCs were validated against tests involving monochromatic waves and morphodynamic bores.

The performance of the technique has been quantified by analysing the restoring of quiescence after a monochromatic wave enters and is reflected back out of the domain. Local (max and min) and global (RMSE) errors for water surface perturbation and velocity reduce with decreasing incoming wave steepness and with increasing relative wavenumber. Nearly in all considered cases, errors are within the 1% threshold, giving evidence of the REBCs effectiveness. Performance improves with increasing wave linearity, indicating that the linearisation of the velocity plays a key role in the accuracy of the conditions. This is also confirmed in the analysis of the absorption defect for morphodynamic bore test, in which overall REBCs performed reasonably well.

The use of the proposed boundary conditions for engineering applications implies the possibility of simulating the reflection of long sequence of waves without altering the physical processes involved. It has been shown that the hydrodynamics and bed evolution in the case of monochromatic wave trains over a mobile bed are not perturbed by the errors in absorption at the seaward boundary, giving confidence in the capability of the proposed conditions to simulate engineering problems accurately.

Finally, note that the REBCs do not depend on the particular adopted sediment transport formula, so that more sophisticated closures for the instantaneous sediment transport can be used.

Appendix A. TVD-MacCormack scheme

In vectorial form, system (1) reads

$$\frac{\partial \mathbf{w}}{\partial t} + \frac{\partial \mathbf{F}(\mathbf{w})}{\partial x} = \mathbf{S}, \tag{A.1}$$

where

$$\mathbf{w} = [h,\ \ hu,\ \ z_b]^T,$$
$$\mathbf{F} = \left[hu,\ \ hu^2 + \frac{1}{2}gh^2,\ \ \xi q_s\right]^T \text{ and}$$
$$\mathbf{S} = \left[0,\ \ -gh\frac{\partial z_b}{\partial x},\ \ 0\right]^T.$$

The TVD-MCC consists of three steps:

$$\mathbf{w}_m^p = \mathbf{w}_m^n - \frac{\Delta t}{\Delta x}\left(\mathbf{F}_{m+1}^n - \mathbf{F}_m^n\right) + \Delta t \mathbf{S}_{m+\frac{1}{2}}^n, \tag{A.2}$$

$$\mathbf{w}_m^c = \mathbf{w}_m^n - \frac{\Delta t}{\Delta x}\left(\mathbf{F}_m^p - \mathbf{F}_{m-1}^p\right) + \Delta t \mathbf{S}_{m-\frac{1}{2}}^p, \tag{A.3}$$

$$\mathbf{w}_m^{n+1} = \frac{1}{2}(\mathbf{w}_m^p + \mathbf{w}_m^c) + \left(\mathbf{D}_{m+\frac{1}{2}}^n - \mathbf{D}_{m-\frac{1}{2}}^n\right), \tag{A.4}$$

where $\mathbf{D}$ is the TVD-function. n and m identify the values at the generic time step n at cell m, p and c the predictor and the corrector stages in the order. The adopted TVD-function $\mathbf{D}$ is

$$\mathbf{D}_{m+\frac{1}{2}}^n = \frac{\Delta t}{2\Delta x}\sum_{k=1}^{3}\left[(\alpha_k \Psi(\bar{\lambda}_k))(1-|\nu_k|)(1-\Phi(\theta_k))\bar{\mathbf{e}}_k\right]_{m+\frac{1}{2}}^n, \tag{A.5}$$

with the overbar indicating values at $m+\frac{1}{2}$, where Roe averages are considered. $\bar{\lambda}_k$ is k-th eigenvalue of Jacobian matrix $\widehat{\mathbf{J}}(\mathbf{w})$ of the system (A.1) when expressed in quasi-linear form (Castro Díaz et al., 2008) and $\bar{\mathbf{e}}_k$ the corresponding right eigenvector.
α_k is the k-th wave strength, given by:

$$\alpha_{k,m+\frac{1}{2}} = \frac{\Delta h(\bar{\lambda}_a\bar{\lambda}_b - \bar{u}^2 + \bar{c}^2) + \Delta(hu)(2\bar{u} - \bar{\lambda}_a - \bar{\lambda}_b) + \Delta z_b\,\bar{c}^2}{(\bar{\lambda}_k - \bar{\lambda}_a)(\bar{\lambda}_k - \bar{\lambda}_b)}, \tag{A.6}$$

with $a \neq k \neq b$ and $c = \sqrt{gh}$.
Moreover, $\Psi(\bar{\lambda}_k)$ is the entropy correction to $\bar{\lambda}_k$. Due to the work of Harten and Hyman (1983), its expression is

$$\begin{array}{ll} \Psi(\bar{\lambda}_k) = |\bar{\lambda}_k| & \text{if } |\bar{\lambda}_k| \geq \delta, \\ \Psi(\bar{\lambda}_k) = \delta & \text{if } |\bar{\lambda}_k| < \delta, \end{array} \tag{A.7}$$

where δ is a small non-negative number determined by the relationship below

$$\delta = \max(0, \bar{\lambda}_k - \lambda_{k,m}, \lambda_{k,m+1} - \bar{\lambda}_k). \tag{A.8}$$

Finally, $\nu_k = \bar{\lambda}_k(\Delta t/\Delta x)$ is the local Courant Number and $\Phi(\theta_k)$ is the flux limiter. In this paper the following Minmod flux limiter is employed:

$$\Phi(\theta_k) = \max\left(0, \min(\theta_k, 1)\right), \tag{A.9}$$

with θ_k being a smoothness ratio defined by

$$\theta_{k,m+\frac{1}{2}} = \frac{\alpha_{k,\dot{m}+\frac{1}{2}}}{\alpha_{k,m+\frac{1}{2}}} \quad \text{where} \quad \dot{m} = m - sgn\left(\bar{\lambda}_k\right). \tag{A.10}$$

Appendix B. Open problem at reflective boundary

In the morphodynamic bore test, it has been observed that at last two cells next to the reflective (right) boundary the bed level profile does not reach the final correct value and the water free surface returns to be flat, consistently with quiescent water (see Figure B.13).

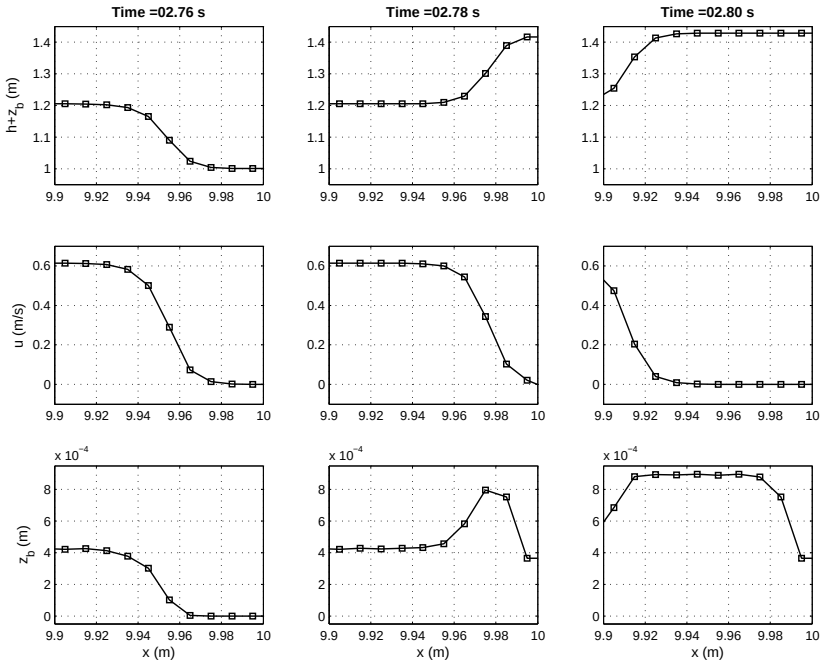

Figure B.13: Morphodynamic bore - profiles in the proximity of the reflective boundary at three different times around time of incoming bore reflection therein - $h_0 = 1.0\ m$ and $H = 0.20\ m$. Top panels: water surface ($h + z_b$); mid panels: velocity (u); bottom panels: bed level (z_b).

The authors studied this error further through a number of additional simulations.

Firstly, suspecting of the predictor-corrector procedure embedded in the TVD-MCC, the test was repeated applying the well-known Lax-Wendroff scheme (Hudson, 2001) to the last cell of the domain. However, very similar results to those previously achieved were obtained.

Secondly, with respect to the numerical settings, it was tried to increase the space resolution and to reduce the Courant Number, but the results did not improve.

Thirdly, the authors switched from the (standard) Minmod flux limiter in the TVD function (A.5) to the Superbee and van Leer ones (Sweby, 1984). Results demonstrated a partial dependency of the solution on the particular flux limiter

but none of them could fix the error.

To the best of authors' knowledge, no other result for the reflection of a bore over a mobile bed with NLSWEs-Exner solvers could be found in the literature. However, the present issue shows strong analogies with a numerical error found in gas dynamics simulations using shock-capturing schemes, known as 'overheating' (Donat & Marquina, 1996). It was observed in a wide range of methods, both Eulerian and Lagrangian (Zaide & Roe, 2012), and it seems to be still an open problem in that research field (Liou, 2012).

The authors can highlight some points of interest about this numerical error.

Firstly, the last cell inside the domain and the boundary one have opposite but same absolute value velocities at any time. This means that a 'sonic point' for the bed level eigenspeed is always located at the reflective boundary and this completely agrees with what experienced in gas dynamics (Toro, 1999).

Secondly, the TVD-MCC actually can not resolve a sharp 'theoretical' discontinuity, as all shock-capturing schemes, hence the morphodynamic bore is represented as a smeared transition over more than two cells. Some researchers in the gas dynamics field (Menikoff, 1994) argued that this artificial shock width causes the mismatch.

Thirdly, the error could be related to the 'nature' of the sediment conservation equation, in particular to its non-linearity and to that of the whole system (Zaide & Roe, 2012; Zaide, 2012).

About this last point and for the sake of numerical speculation, some simulations were conducted adopting a linear and a quadratic relationship in u for q_s, instead of the standard cubic one (2). Interestingly, the error disappears with the linear formula, while persists with the quadratic one.

In addition to this, no sonic point takes place at the reflective boundary using the quadratic formula, therefore it does not produce the error.

On the other hand, the smearing of the bore is apparent even with the linear formula and this implies that the artificial bore width does not cause the mismatch by itself.

To summarise, the error at the reflective boundary appears to be first of all related to the non-linearity of the sediment conservation equation and subsequently probably affected by the bore smearing.

Acknowledgements

Giorgio Incelli and co-authors would like to express their gratitude to The University of Nottingham for providing financial support. Riccardo Briganti is supported by the EPSRC Career Acceleration Fellowship (EP/I004505/1). Results using the WAF method solver are courtesy of Mr Benjamin Tatlock.

References

Abramowitz, M., & Stegun, I. A. (1972). *Handbook of mathematical functions: with formulas, graphs, and mathematical tables*. 55. New York: Courier Dover Publications.

Briganti, R., & Dodd, N. (2009). Shoreline motion in nonlinear shallow water coastal models. *Coastal Engineering*, *56*, 495–505. doi:10.1016/j.coastaleng.2008.10.008.

Briganti, R., Dodd, N., Kelly, D. M., & Pokrajac, D. (2012a). An efficient and flexible solver for the simulation of the morphodynamics of fast evolving flows on coarse sediment beaches. *International Journal for Numerical Methods in Fluids*, *69*, 859–877. doi:10.1002/fld.2618.

Briganti, R., Dodd, N., Pokrajac, D., & O'Donoghue, T. (2012b). Numerical and experimental description of the flow, boundary layer and bed evolution in bore-driven swash on a coarse sediment beach. In P. Lynett, & J. McKee Smith (Eds.), *Proceedings of 33rd International Conference on Coastal Engineering, Santander, Spain, 1-6 July, 2012*. Coastal Engineering Proceedings volume 33. doi:10.9753/icce.v33.currents.33.

Castro Díaz, M. J., Fernández-Nieto, E. D., & Ferreiro, A. M. (2008). Sediment transport models in shallow water equations and numerical approach by high order finite volume methods. *Computers & Fluids*, *37*, 299–316. doi:10.1016/j.compfluid.2007.07.017.

Dodd, N., Stoker, A. M., Calvete, D., & Sriariyawat, A. (2008). On beach cusp formation. *Journal of Fluid Mechanics*, *597*, 145–169. doi:10.1017/S002211200700972X.

Donat, R., & Marquina, A. (1996). Capturing shock reflections: an improved flux formula. *Journal of Computational Physics*, *125*, 42–58. doi:10.1006/jcph.1996.0078.

van Dongeren, A. R., & Svendsen, I. A. (1997). Absorbing-generating boundary condition for shallow water models. *Journal of Waterway, Port, Coastal and Ocean Engineering*, *123*, 303–313. doi:10.1061/(ASCE)0733-950X(1997)123:6(303).

Fraccarollo, L., & Capart, H. (2002). Riemann wave description of erosional dam-break flows. *Journal of Fluid Mechanics*, *461*, 183–228. doi:10.1017/S0022112002008455.

Hanson, H., & Kraus, N. C. (1989). *GENESIS: Generalized Model for Simulating Shoreline Change. Report 1. Technical Reference*. Technical Report 1 DTIC Document.

Hudson, J. (2001). *Numerical tecniques for morphodynamical modelling*. Ph.D. thesis University of Reading.

Hudson, J., Damgaard, J., Dodd, N., Chesher, T., & Cooper, A. (2005). Numerical approaches for 1D morphodynamic modelling. *Coastal Engineering*, *52*, 691–707. doi:10.1016/j.coastaleng.2005.04.004.

Hudson, J., & Sweby, P. K. (2003). Formulations for numerically approximating hyperbolic systems governing sediment transport. *Journal of Scientific Computing*, *19*, 225–252. doi:10.1023/A:1025304008907.

Kelly, D. M., & Dodd, N. (2009). Floating grid characteristics method for unsteady flow over a mobile bed. *Computers & Fluids*, *38*, 899–909. doi:10.1016/j.compfluid.2008.09.011.

Kelly, D. M., & Dodd, N. (2010). Beach-face evolution in the swash zone. *Journal of Fluid Mechanics*, *661*, 316–340. doi:10.1017/S0022112010002983.

Kobayashi, N., Otta, A. K., & Roy, I. (1987). Wave reflection and run-up on rough slopes. *Journal of Waterway, Port, Coastal and Ocean Engineering*, *113*, 282–298. doi:10.1061/(ASCE)0733-950X(1987)113:3(282).

Landry, B. J., Hancock, M. J., & Mei, C. C. (2007). Note on sediment sorting in a sandy bed under standing water waves. *Coastal Engineering*, *54*, 694–699. doi:10.1016/j.coastaleng.2007.02.003.

Liou, M.-S. (2012). Unresolved problems by shock capturing: Taming the overheating problem. In *Proceedings of 7th International Conference on Computational Fluid Dynamics, Big Island, Hawaii, 9-13 July, 2012*.

Menikoff, R. (1994). Errors when shock waves interact due to numerical shock width. *SIAM Journal on Scientific Computing*, *15*, 1227–1242. doi:10.1137/0915075.

Roelvink, D., Reniers, A., van Dongeren, A. P., van Thiel de Vries, J., McCall, R., & Lescinski, J. (2009). Modelling storm impacts on beaches, dunes and barrier islands. *Coastal Engineering*, *56*, 1133–1152. doi:10.1016/j.coastaleng.2009.08.006.

Savary, C., & Zech, Y. (2007). Boundary conditions in a two-layer geomorphological model. application to a hydraulic jump over a mobile bed. *Journal of Hydraulic Research*, *45*, 316–332. doi:10.1080/00221686.2007.9521766.

Svendsen, I. A. (2005). *Introduction to nearshore hydrodynamics* volume 24 of *Advanced Series on Ocean Engineering*. Singapore: World Scientific Publishing.

Sweby, P. K. (1984). High resolution schemes using flux limiters for hyperbolic conservation laws. *SIAM Journal on Numerical Analysis*, *21*, 995–1011. doi:10.1137/0721062.

Toro, E. F. (1999). *Riemann solvers and numerical methods for fluid dynamics* volume 16. (2nd ed.). Springer-Verlag.

Toro, E. F. (2001). *Shock-capturing methods for free-surface shallow fluids*. Chichester: John Wiley & Sons.

Wei, G., Kirby, J. T., & Sinha, A. (1999). Generation of waves in Boussinesq models using a source function method. *Coastal Engineering*, *36*, 271–299. doi:10.1016/S0378-3839(99)00009-5.

Zaide, D. W., & Roe, P. L. (2012). Flux functions for reducing numerical shockwave anomalies. In *Proceedings of 7th International Conference on Computational Fluid Dynamics, Big Island, Hawaii, 9-13 July, 2012*.

Zaide, D. W.-M. (2012). *Numerical Shockwave Anomalies*. Ph.D. thesis The University of Michigan.

Zhu, F. (2012). *1D morphodynamical modelling of swash zone beachface evolution*. Ph.D. thesis The University of Nottingham.

Zhu, F., & Dodd, N. (2013). Net beach change in the swash zone: A numerical investigation. *Advances in Water Resources*, *53*, 12–22. doi:10.1016/j.advwatres.2012.10.002.

Zhu, F., Dodd, N., & Briganti, R. (2012). Impact of a uniform bore on an erodible beach. *Coastal Engineering*, *60*, 326–333. doi:10.1016/j.coastaleng.2011.08.006.